Microwave-Assisted Synthesis of SnO₂ Nanosheets Photoanodes for Dye-Sensitized Solar Cells

Yajie Wang,[†] Jianjun Tian,[†,‡] Chengbin Fei,[†] Lili Lv,[†,‡] Xiaoguang Liu,[†,‡] Zhenxuan Zhao,[†] and Guozhong Cao*,[†,§]

[†]Beijing Institute of Nanoenergy and Nanosystems, Chinese Academy of Sciences, Beijing, 100083, People's Republic of China
[‡]Advanced Material and Technology Institute, University of Science and Technology, Beijing, 100083, People's Republic of China
[§]Department of Materials and Engineering, University of Washington, Seattle, Washington 98195-2120, United States

ABSTRACT: SnO₂ nanosheets were synthesized using microwave-assisted hydrothermal growth and used as photoanodes for dye-sensitized solar cells (DSCs) and demonstrated much better photoelectrical energy conversion performance than that of SnO₂ synthesized with traditional hydrothermal growth, due to a significant decrease in charge diffusion distance and charge recombination. The crystallinity and microstructure of the samples were investigated by means of X-ray diffraction (XRD), scanning, and transmission electron microscopy (SEM/TEM). The specific surface area and pore size distribution were determined by means of nitrogen sorption isotherms. The interfacial charge transfer process and the charge recombination were characterized by electrochemical impedance spectrum (EIS) and intensity modulated photocurrent/photovoltage spectra (IMPS/IMVS) measurements. The DSCs assembled with SnO₂ nanosheets as photoanodes from microwave-assisted synthesis exhibited much enhanced energy conversion efficiency, which is attributed to a higher open-circuit voltage due to less charge recombination, and a large short-circuit current density due to both large surface area and effective light scattering effect.
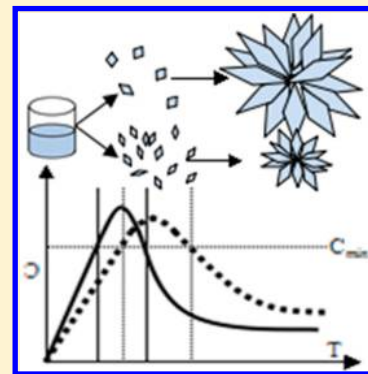
INTRODUCTION

In the past decades, since the demonstration of titanium dioxide (with a band gap of 3.2 eV) nanoparticles coated with dye molecules to convert solar energy to electricity in a simple and low-cost way by O'Regan and Grätzel,[1] synthesis of wide band gap oxide nanomaterials with controlled shapes and sizes has been an extensive research area for dye-sensitized solar cells (DSCs).[2,3] Improving solar energy conversion efficiency while at the same time reducing costs by controlling nanomaterials' shapes, sizes, and other properties has become a significant domain.[4] Although a record power conversion efficiency of higher than 13% has been achieved with use of TiO₂ nanoparticle films through the molecular engineering of porphyrin sensitizers in DSCs,[5] further improvement with TiO₂ is difficult due to its relatively small electron mobility.[6,7] SnO₂ as a semiconducting oxide when used as a photoanode in DSCs promises many advantages: (1) Compared to the poor electron mobility of anatase TiO₂ ($0.1-1$ cm² V⁻¹ s⁻¹), it has much higher electron mobility ($100-200$ cm² V⁻¹ s⁻¹).[8–10] (2) It has a larger band gap (3.6 eV) and a more-negative conduction band minimum (-4.8 eV) than that of anatase TiO₂ (-4.2 eV), and thus can enhance light harvesting in the near-infrared spectral region when combined with a small band gap sensitizer. (3) There are fewer oxidative holes in the valence band, contributing to long-term stability of DSCs.[11] In fact, SnO₂ as a possible replacement of TiO₂ photoanode in DSCs with various morphologies, such as nanoparticles,[12,13] nanofibers,[14] nanowires,[15] nanotubes,[16] and hollow nanospheres,[17–20] has been successfully synthesized and charac-

terized. For example, Cheng et al.[21] reported the synthesis of single-crystalline SnO₂ nanorods with small size (15–20 nm in length and 2.5–5 nm in diameter) by hydrothermal treatment of TiCl₄. Wu et al.[22] prepared 3D hierarchical SnO₂ nanostructures composed of 2D nanosheets. TiO₂-coated multilayered SnO₂ hollow microspheres have achieved 5.65% photoconversion efficiency.[23]

Among various techniques used for SnO₂ synthesis, hydrothermal growth is one of the most common methods, which can form the desired size and morphology by manipulating the reactant ratio and reaction parameters.[24] In contrast to the cumbersome and long-running processing nature of hydrothermal synthesis, microwave-assisted synthesis offers rapid processing speed, homogeneous heating, and simple control of processing conditions, and thus has attracted much attention in the past few years.[25] Ding et al.[26] reported the synthesis TiO₂ nanocrystals via a microwave-assisted process and demonstrated that anatase nanocrystals are highly crystalline, low in Ti³⁺ defect, and free of aggregation. Hu et al.[27] synthesized the linked single-crystalline ZnO rods using the microwave-assisted process, demonstrating that microwave-assisted solution-phase routes can fabricate the linked ZnO rods without templates, seeds, or surfactants and are suitable for large-scale production. The possibility to alter the physical and chemical properties of nanoscale materials through varying the crystal shape and size is

a primary research.[28−30] Chemical synthesis in a liquid phase through microwave irradiation mainly involves dipolar polarization and ionic conduction heating mechanisms.[25] The use of microwave-assisted synthesis of SnO_2 is assumed to lead to different properties compared with hydrothermal synthesis.

This paper reports a microwave-assisted synthesis of assembled SnO_2 nanosheets and their characterization and application as photoanodes in DSCs. The assembled SnO_2 nanosheets photoanode, with large specific surface area, effective light-scattering, and an easy path for electron transport with long lifetime, demonstrated appreciably increased short-circuit photocurrent density, reduced charge recombination, and consequently high power conversion efficiency. The possible mechanism was discussed about the difference between SnO_2 structures of microwave-assisted synthesis and hydrothermal synthesis.

■ EXPERIMENTAL METHODS

Synthesis of SnO_2 Nanosheets. *Microwave-Assisted Aqueous Method.* First, $SnCl_2 \cdot 2H_2O$ (0.90 g, 4.0 mmol) and $Na_3C_6H_5O_7 \cdot 2H_2O$ (2.94 g, 10 mmol) were dissolved in distilled water (10 mL) and stirred for 5 min. Then NaOH (0.2 M, 10 mL) was added to the above solution with continuous stirring to form a homogeneous solution. The solution was transferred to a 35 mL reaction tube and reactor cavity of CEM Discover microwave system. The synthesis parameters were set as T = 180 °C, dwell time = 2 h, power = 120 W, and pressure = 17 bars. The obtained precipitate was separated by centrifugation at 8000 rpm for 30 min and rinsed 3 times with distilled water and 3 times with acetone. Finally the product was dried under vacuum at room temperature overnight. Calcination was conducted in an electrical furnace in air at 450 °C for 4 h with a heating rate of 5 deg/min and cooled in the static air.

Hydrothermal Method. In a typical experiment,[31] $SnCl_2 \cdot 2H_2O$ (4.0 mmol) and $Na_3C_6H_5O_7 \cdot 2H_2O$ (10 mmol) were dissolved in distilled water and stirred for 5 min. Then NaOH (0.2 M) aqueous solution was added to the above solution with continuous stirring to form a homogeneous solution. The mixture (10 mL) was transferred to a 25 mL Teflon-lined stainless steel autoclave and then heated in an oven at 180 °C for 12 h with a heating rate of 5 deg/min. The obtained precipitate was separated by centrifuge at 8000 rpm for 30 min and rinsed 3 times with distilled water and 3 times with acetone. Finally the product was dried at room temperature overnight. Calcinations were conducted in an electrical furnace in air at 450 °C for 4 h with a heating rate of 5 deg/min and cooled in the static air.

Preparation of SnO_2 Paste. SnO_2 powders (0.18 g) were placed in an agate mortar, and 5.0 mL of ethanol was added dropwise into the mortar. The SnO_2 powders were ground for 30 min. The ground SnO_2 was then transferred to a solution of terpineol (0.73 g) and ethyl cellulose (0.09 g) in a 10 mL beaker under magnetic stirring. The dispersion was homogenized by means of ultrasonic and magnetical stirring overnight.

Fabrication of DSCs. A layer of SnO_2 film was prepared by the doctor blade technique. The film was sintered at 500 °C for 60 min in air to remove any organic compounds. The resulting SnO_2 films were then immersed in 100 mM $TiCl_4$ aqueous solution in a closed vessel at 70 °C for 30 min. Then the films coated with $TiCl_4$ aqueous were annealed at 500 °C for 30 min before dye sensitization. The electrodes with a cell area of 0.25 cm^2 were immersed in a 0.25 mM N719 sensitizer dye for 18 h.

The counter-electrodes were Pt coated FTO, and the electrolyte was contained I^-/I^{3-} redox. The DSCs with $TiCl_4$ treatment and without $TiCl_4$ treatment were designed by SnO_2 (hydrothermal), SnO_2 (microwave), and SnO_2 (hydrothermal)-untreated, and SnO_2 (microwave)-untreated.

Characterization. X-ray diffraction (XRD) measurements were conducted on an X'Pert PROS (Philips Co.) with a radiation of Cu Kα (λ = 1.54060 Å). Scanning electron microscopy (SEM) measurements were undertaken by using a field emission environmental scanning electron microscope (SU8020, Hitachi Co.). A transmission electron microscope (TEM) and a high-resolution TEM (HRTEM) were used to study the morphology and microstructure of the materials by a JEM-2010 (JEOL) instrument. N_2 adsorption−desorption isotherms were recorded on an ASAP2020 instrument (Micromeritics Co.), and the specific surface areas (SBET) were calculated with the BET equation. The desorption isotherm was used to determine the pore size distribution, using the Barret−Joyner−Halender (BJH) method. The concentration of desorbed dye in film was calculated from UV−vis absorption spectra (UV-3600, Shi-madzu). The photovoltaic performance of DSCs was measured under a solar simulator (Oriel Sol 3A Solar Simulator, 94063A, Newport Stratford Inc.), equipped with a 300 W xenon lamp (Newport) and a Keithley digital source meter (Keithley, 2400) controlled by Testpoint software. The irradiation intensity was calibrated to 100 mW·cm^{-2} with a standard reference crystalline silicon solar cell (Newport, Stratford Inc., 91150 V). The incident monochromatic photon-to-electron conversion efficiency (IPCE), plotted as a function of excitation wavelength and EIS measurements, was recorded by IM6ex (Germany, Zahner Company), using light emitting diodes (λ = 455 nm) driven by Expot (Germany, Zahner Company). The EIS data were fit to the equivalent circuits by using Zview software (Scribner Associates). Impedance measurements were carried out under illumination from LED. The intensity modulated photocurrent/photovoltage spectra (IMPS/IMVS) measurements were carried out with the same instrument used for EIS measurements. The LED provided both dc and ac components of the illumination.

■ RESULTS AND DISCUSSION

Characterization of SnO_2 Nanosheets. Figure 1 shows the XRD patterns of SnO_2 (hydrothermal) and SnO_2 (microwave), both of which have the tetragonal rutile structure with lattice constants of a = 4.738 Å and c = 3.187 Å (JCPDS card 41−1445). No other impurity crystal is detectable, which suggests that both microwave-assisted growth and hydrothermal growth can effectively form high purity tetragonal rutile SnO_2 crystal.

Figure 2 gives the SEM images showing (a, b) SnO_2 (hydrothermal) nanostructure and (c, d) SnO_2 (microwave) nanostructure. Both methods can form SnO_2 nanosheets with almost identical appearance. However, a closer look reveals the appreciable size difference of nanosheets formed by the two methods. Microwave-assisted synthesis resulted in smaller SnO_2 nanosheets than those by hydrothermal growth. The SnO_2 nanosheets grown by the hydrothermal method have a thickness of 20−25 nm and a length of 270 nm, while the SnO_2 nanosheets grown by microwave-assisted synthesis have a thickness of 10 nm and a length of 160 nm approximately. The high-resolution TEM image (Figure 2, b and d inset) indicates that the assembled SnO_2 nanosheets have a lattice spacing of
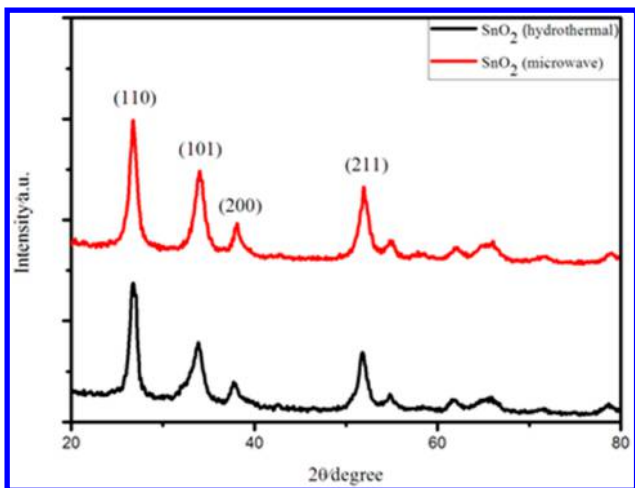
Figure 1. XRD patterns of SnO₂ (hydrothermal) and SnO₂ (microwave) powders.

Figure 3. Illustration of the process of nucleation and subsequent growth where region II is the nucleation zone and region III is the growth zone (dash line: lower ramping rate; solid line: higher ramping rate).

Scheme 1. Schematic of the Formation Processes for the SnO₂ Nanostructure, Illustrating the Differences between Hydrothermal Growth and Microwave-Assisted Synthesis

0.335 and 0.237 nm, corresponding to the (110) lattice plane and the (200) lattice plane of tetragonal rutile SnO_2, respectively.

Figure 3 illustrates the nucleation and growth processes influenced by high and low ramping and cooling rates, and the growth process generally can be divided into three regions.[32] First, there is no nucleation before the concentration reaches the minimum supersaturation required for nucleation (cf. Region I). Once homogeneous nucleation starts, the nucleus growth starts concurrently and very rapidly (cf. Region II).[33] When the concentration falls below a critical nucleation concentration, nucleation stops but growth continues (cf. Region III).

Scheme 1 is the proposed schematic illustration of the formation process for the SnO₂ nanostructure. Nanoparticles are formed by nucleation at a different rate at the beginning of the hydrothermal or microwave synthesis process. The
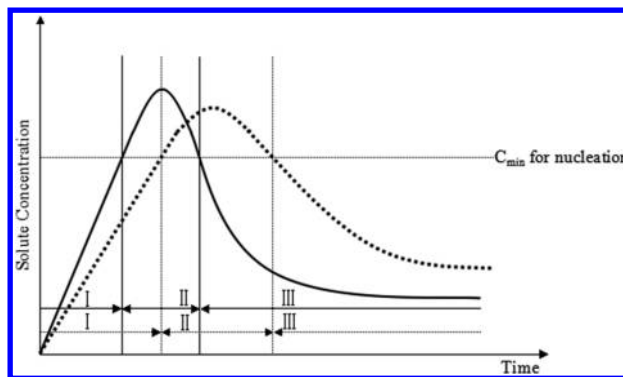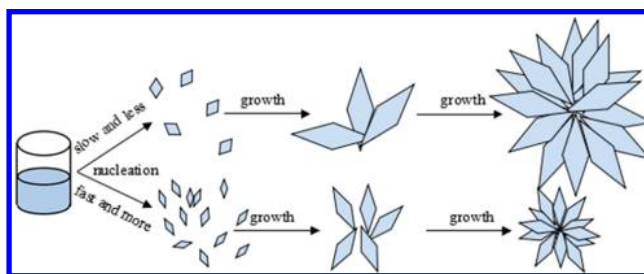
microwave synthesis process can reach the reaction temperature in 3 min, while it needs a few hours in the hydrothermal growth process. The nucleation speed is affected by the concentration and temperature. Hydrothermal growth is a slow-heat process, thus the solution reaches supersaturation after a long time and the supersaturation is low leading to a
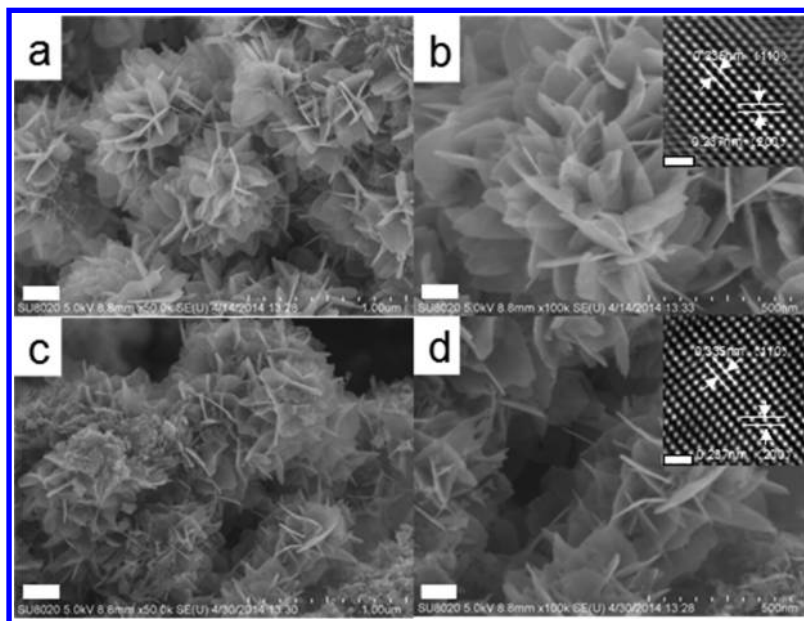

Figure 2. SEM images of (a, b) SnO₂ (hydrothermal) nanostructure and HRTEM images (inset), and SEM images of (c, d) SnO₂ (microwave) nanostructure and HRTEM images (inset). The scale bars in SEM images of parts a and c represent 200 nm. The scale bars in SEM images of parts b and d represent 100 nm. The scale bars in HRTEM figures represent 1 nm.

wide size distribution of initial nuclei. While microwave-assisted synthesis raised the solution to a desired temperature in just a few minutes, it leads to the creation of abrupt supersaturation resulting in a very high nucleation density in a very short time. During and/or immediately after the initial nucleation, the nuclei or small particles form aggregates. Because of the difference in heating mode between hydrothermal method and microwave-assisted synthesis, the microwave method can form more nuclei with a narrower size distribution due to very high heating rate and homogeneous temperature distribution compared to the hydrothermal method leading to the formation of fewer nuclei with broader size distribution. Small particles aggregate to form the core of the flower-like structure and grow preferentially with growth inhibition in the [0 0 1] direction, leading to the formation of large, but thin, nanosheets.[31] Therefore, SnO_2 (hydrothermal) formed big nanosheets, while SnO_2 (microwave) had small length and thin thickness nanosheets.

The assembled SnO_2 (hydrothermal) and SnO_2 (microwave) nanosheets were further characterized by means of nitrogen sorption isotherms at 77 K, and the corresponding pore size distribution is presented in Figure 4. It is found that the SnO_2
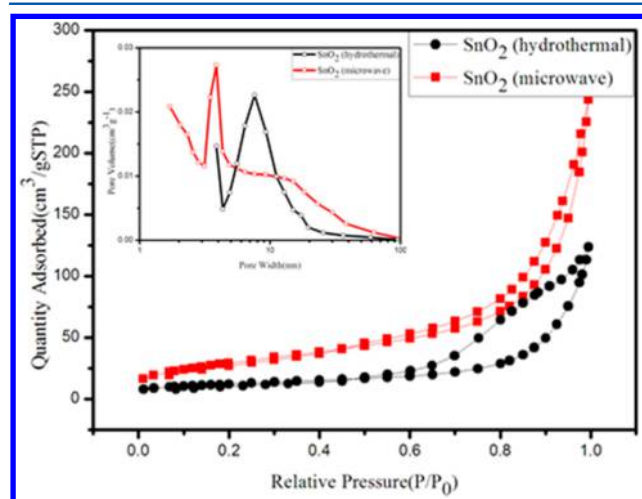

Figure 4. Nitrogen adsorption and desorption isotherms at 77 K, and the pore size distribution (inset) of SnO_2 (hydrothermal) and SnO_2 (microwave) powders.

(microwave) have a BET surface area of 107.5 m^2/g with an average Barret−Joyner−Halenda (BJH) pore diameter of 10.5 nm and a pore volume of 0.41 cm^3/g while the SnO_2(hydrothermal) have a 42.6 m^2/g BET surface area with a BJH pore diameter of 10.5 nm and a 0.22 cm^3/g pore volume.

Owing to the size and surface area differences between use of the hydrothermal method and the microwave-assisted approach to form the SnO_2 nanostructure, it has a strong effect on the amount of dye absorption. Consequently the amount of dye absorption influences the performance of DSCs. Thus, the curves of dye absorption can be seen in Figure 5 and details summarized in Table 1. The SnO_2 (microwave) film provides a much higher dye loading of 2.61 $m^2 g^{-1} \times 10^{-7}$ mol cm^{-2}, while that for the SnO_2 (hydrothermal) film is only 1.62 $m^2 g^{-1} \times 10^{-7}$ mol cm^{-2}. The improved dye loading can enhance the light harvesting efficiency, thereby the photocurrent density, and finally the cell conversion efficiency. According to the BET surface area data, the SnO_2 (microwave) sample has 2.5 times larger surface area than the SnO_2 (hydrothermal) sample,
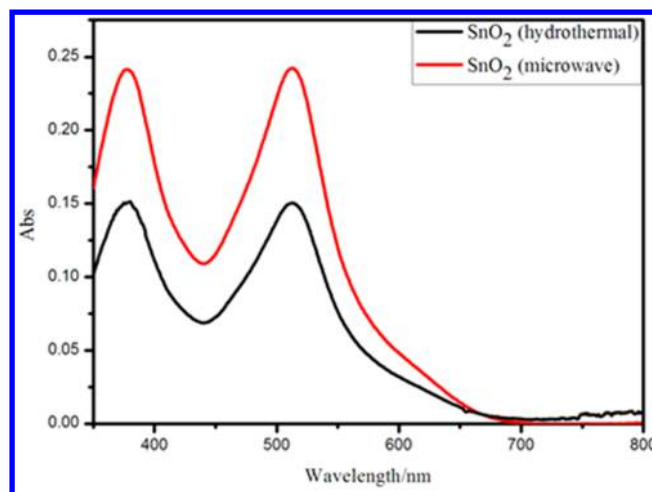

Figure 5. UV−vis absorption spectra of dyes unloaded from SnO_2 (hydrothermal) and SnO_2 (microwave) photoanodes.

whereas it has 1.6 times more dye loading than SnO_2 (hydrothermal). In theory, the value of surface area has the same effect on the amount of dye absorption. Here are two possible reasons for the differences between BET surface area data and dye loading data: (1) Samples used in the UV−vis absorptions spectra of dyes detached from SnO_2 have been treated with 100 mM $TiCl_4$ aqueous solution, hence TiO_2 can alter the surface area and influence the dye adsorption. There are different amounts of TiO_2 adsorbed on the surface of SnO_2 because large surface area favors more TiO_2 deposition. (2) The same volume of the SnO_2 pastes with different pore volume leads to a different weight of two SnO_2 pastes. Although the SnO_2 (microwave) sample has a 2.5 times larger surface area of 107.5 m^2/g than the 42.6 m^2/g of the SnO_2 (hydrothermal) sample, the effective exposure area (S_{BET}/pore volume) has small increases in fact. This is what causes the amount of dye adsorption to not be equal to the BET surface area. These two crucial reasons affect the radio of BET surface area and the amount of dye adsorption.

The light scattering ability of films was measured by the UV−vis diffuse reflectance spectroscopy. As shown in Figure 6, the diffuse reflection of the SnO_2 (microwave) film, which was almost 55%, is much higher than that of the SnO_2 (hydrothermal) film, which was 27%, at 513 nm wavelength.

Characterization of Photovoltaic Properties of DSCs. The incident photon-to-current conversion efficiency (IPCE) spectra from the cells are characterized and shown in Figure 7. The incident photon-to-current conversion efficiency clearly indicates that SnO_2 (microwave) with almost 40% is much higher than SnO_2 (hydrothermal) with 30%. Despite the incident photon-to-current conversion efficiency, the SnO_2 (microwave) electrode has improved compared with SnO_2 (hydrothermal), but it is still a bit low because the value of IPCE is the comprehension result, related to the light harvesting efficiency, electron injection efficiency, dye regeneration efficiency, and charge collection efficiency.[34]

To investigate the interfacial charge transfer process in SnO_2 (hydrothermal) and SnO_2 (microwave) film electrodes, electrochemical impedance spectroscopy (EIS) measurements are employed in the frequency range of 0.1 Hz to 100 kHz. Figure 8 shows the Nyquist plots of SnO_2 (hydrothermal) and SnO_2 (microwave) measured at forward bias of the open-circuit voltage under 100 mW cm^{-2} and the equivalent circuit, inset.

Table 1. Comparison of BET Surface Area (S_{BET}), BJH Pore Diameter, Pore Volume, and the Amount of Dye Loaded in SnO$_2$ (Hydrothermal and Microwave) Nanostructure Photoanodes

DSCs	S_{BET} (m^2 g^{-1})	pore diameter (nm)	pore vol (cm^3/g)	dye loading ($\times 10^{-7}$ mol cm^{-2})
SnO$_2$ (hydrothermal)	42	10	0.22	1.62
SnO$_2$ (microwave)	107	10	0.41	2.61
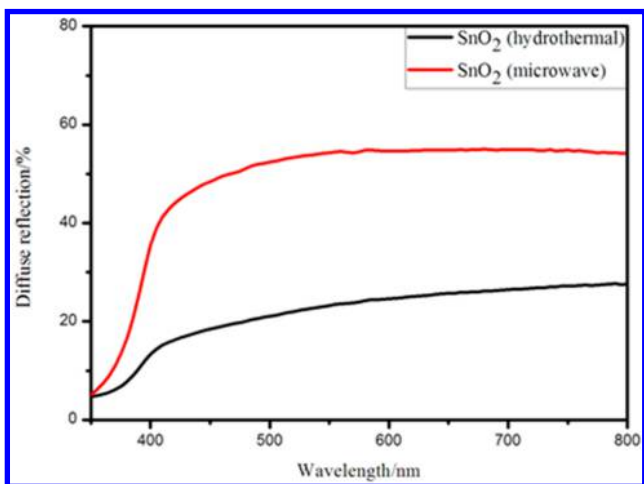
Figure 6. Curves of diffuse reflectance of SnO$_2$ (hydrothermal) and SnO$_2$ (microwave) nanostructure photoanodes without dye loading.
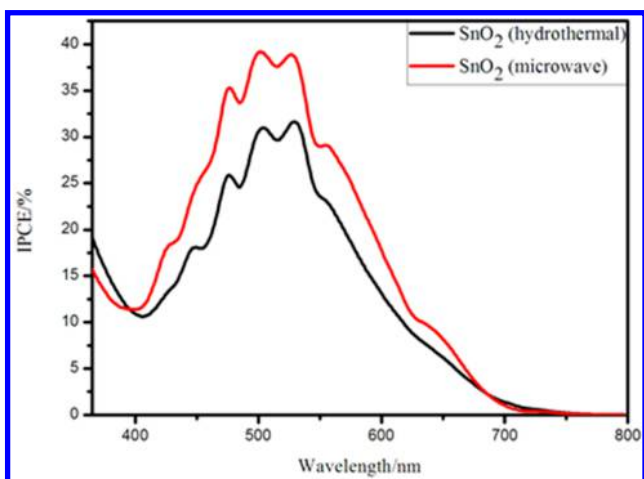
Figure 7. IPCE spectra of DSCs with SnO$_2$ (hydrothermal) and SnO$_2$ (microwave) photoanodes.

Figure 8. Nyquist plots of electrochemical impedance spectra of SnO$_2$ (hydrothermal) and SnO$_2$ (microwave) photoanodes.

The electron transport and charge recombination of the DSCs based on SnO$_2$ (hydrothermal) and SnO$_2$ (microwave) films were further characterized by intensity modulated photocurrent spectroscopy (IMPS) and intensity modulated photovoltage spectroscopy (IMVS). They are conducted under illumination of a LED light source (λ = 530 nm) with different light intensities from 20 to 100 W m^{-2}. In Figure 9, τ_d and τ_r
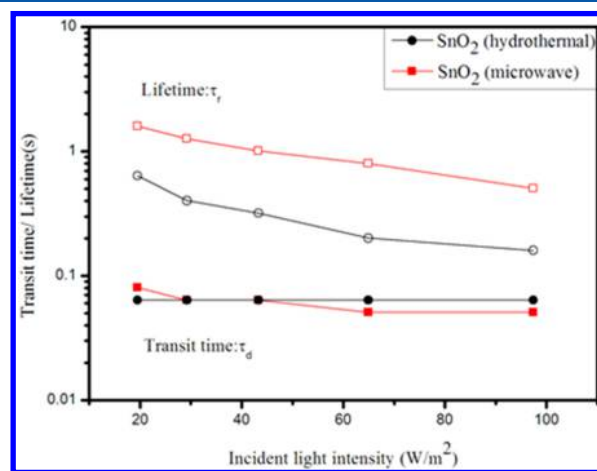
Figure 9. Electron transport time and electron lifetime of the DSCs fabricated with SnO$_2$ (hydrothermal) and SnO$_2$ (microwave) films as a function of the incident light intensity.

From the Nyquist plots the smaller semicircle occurring at higher frequencies represents the parallel connection of charge-transfer resistance (R_k) and the interfacial capacitance (C_k) at the counter electrode/electrolyte interface. The larger one at the lower frequency region is related to the combination of charge-transfer resistance occurring at the oxide/dye/electrolyte interface (R_{pt}) and the chemical capacitance that stands for the change of electron density (C_{pt}). The semicircle of SnO$_2$ (microwave) is larger than that of SnO$_2$ (hydrothermal), probably owing to the reduced electron transfer process in the photoanode. The larger semicircle at lower frequencies of SnO$_2$ (microwave) is much larger than that of SnO$_2$ (hydrothermal). The values of R_{pt} corresponding to SnO$_2$ (hydrothermal) and SnO$_2$ (microwave) are 29Ω and 53Ω, respectively. This is taken as an evidence that SnO$_2$ (microwave) film electrodes have less charge recombination than SnO$_2$ (hydrothermal) photoanodes.

are the electron transit time and the lifetime, which is also the recombination of electrons and electrolyte. Table 2 summarizes the two kinds of film results from the IMPS and IMVS plots under a light intensity of 97 W m^{-2}. τ_d and τ_r can be calculated from the following expression: $\tau_d = {}^1/_2\pi f_d$ and $\tau_r = {}^1/_2\pi f_r$, where f_d and f_r are the characteristic frequency minimum of the IMPS and IMVS imaginary components, respectively, along with the increasing light intensity. The electron diffusion coefficient (D_n) in SnO$_2$ films is described by the analytical expression D_n

Table 2. Detailed IMPS and IMVS Parameters[a]

DSCs	τ_d (ms)	τ_r (ms)	D_n ($\mu m^2 s^{-1}$)	L_n (μm)	λ_{cc} (%)
SnO$_2$ (microwave)	50.7	506	7553	61.8	90
SnO$_2$ (hydrothermal)	63.8	160	6002	31.0	60

[a]Electron transit time (τ_d), electron lifetime (τ_r), electron diffusion coefficient (D_n), electron diffusion length (L_n), and charge-collection efficiency (λ_{cc}) of dye-sensitized solar cells based on SnO$_2$ (hydrothermal) and SnO$_2$ (microwave) under a light intensity of 97 W m^{-2}.

$= d^2/2.35\tau d$,[35,36] where d is the film thickness. Combining the following equations $L_n = (D_n \times \tau_r)^{1/2}$,[37] and $\lambda_{cc} = 1 - \tau_d/\tau_r$,[38] the electron diffusion length (L_n) and charge-collection efficiency (λ_{cc}) can be calculated.

As shown in Figure 9, the SnO$_2$ (microwave) film shows longer lifetimes (τ_r) than the SnO$_2$ (hydrothermal) film. The reasons why the electron lifetime has significantly improved are possibly that (1) the SnO$_2$ from the microwave-assisted synthesis method has smaller nanosheets which can be more easily crystallized at the same sintering temperature and (2) the compact structure of SnO$_2$ from the microwave-assisted synthesis method can greatly reduce the electron recombination because of fewer reactions with iodide ions in the electrolyte. However, in theory, SnO$_2$ from the microwave-assisted synthesis method used to form DSC has a shorter electron lifetime than the SnO$_2$ (hydrothermal) film since a larger surface area would also offer more sites for charge recombination. The positive and negative effects result in the SnO$_2$ (microwave) film having a much longer lifetime than the SnO$_2$ (hydrothermal) film, even triple the lifetime. The τ_d parameter of the SnO$_2$ (microwave) film device DSC is similar to the SnO$_2$ of the hydrothermal method, indicating the transport times of the two cells are parallel. No matter what kind of synthesis method is used to form the assembled SnO$_2$ nanosheets, this will lead to many trapping sites and boundaries due to their hierarchical structures. As a result, these trapping sites of the hierarchical structures give rise to countless trapping/detrapping events. This is the reason why the SnO$_2$ (hydrothermal) film and the SnO$_2$ (microwave) film have similar transport times. L_n represents the average travel distance of electrons before recombining with others. The value of L_n indicates that the injected electron could whether transit to the external effectively. Because the SnO$_2$ (microwave) film has a longer electron lifetime than the SnO$_2$ (hydrothermal) film and a higher diffusion coefficient (D_n), the electron diffusion length (L_n) of the SnO$_2$ (microwave) film is also high. The charge collection efficiency (λ_{cc}) is the integrated result of the competition between the collection of photoinjected electrons and recombination. The calculated charge collection efficiency of the SnO$_2$ (microwave) film is 90%, much more than the 60% of the SnO$_2$ (hydrothermal) film. This can be attributed to the much longer electron lifetime in SnO$_2$ grown with the microwave-assisted synthesis.

Finally, Figure 10 presents the $J-V$ curves of DSC devices with photoanodes made of SnO$_2$ (hydrothermal) and SnO$_2$ (microwave) nanostructures. As shown in Table 3, the photoconversion efficiency of SnO$_2$ (microwave) is 3.34%, enhanced 31% from the photoconversion efficiency of SnO$_2$ (hydrothermal) at 2.55%. The main reason is the improved dye loading, therefore the short-circuit photocurrent density has greatly improved. On the other hand, using the microwave-assisted synthesis method to form the nanostructure can
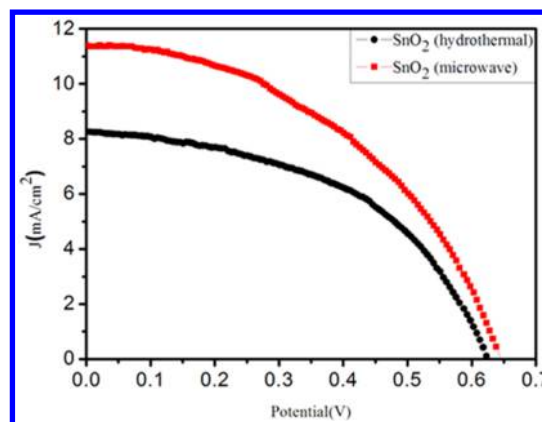

Figure 10. $J-V$ curves of SnO$_2$ (hydrothermal) and SnO$_2$ (microwave) photoanodes.

Table 3. Comparison of Short-Circuit Photocurrent Density (J_{sc}), Open-Circuit Photovoltage (V_{oc}), Fill Factor (FF), and Photoconversion Efficiency (η) for the SnO$_2$ (Hydrothermal) and SnO$_2$ (Microwave) Photoanodes, Respectively

DSCs	J_{sc} (mA/cm^2)	V_{oc} (V)	FF (%)	η (%)
SnO$_2$ (microwave)	11.5	0.65	0.45	3.34
SnO$_2$ (hydrothermal)	8.3	0.63	0.49	2.55

minimize the oversized SnO$_2$ nanosheets from the hydrothermal method. The small nanosheets can shorten the distance between the semiconductor photoanode and the electrolyte, thereby forming a direct path and contact.

■ CONCLUSIONS

Microwave-assisted synthesis was demonstrated to produce SnO$_2$ nanosheets with substantially reduced sheet size as compared with ones synthesized by the SnO$_2$ hydrothermal method. Consequently, dye loading and light scatting in the microwave-assisted synthesized SnO$_2$ nanosheets as photoandes in dye-sensitized solar cells were appreciably enhanced. In addition, microwave-assisted synthesized SnO$_2$ nanosheets have a longer electron lifetime, and less electron recombination than the hydrothermal grown SnO$_2$ electrodes; collectively, the short-circuit photocurrent density has been greatly increased.

■ AUTHOR INFORMATION

Corresponding Author
*E-mail: gzcao@u.washington.edu. Phone: 206-616-9084. Fax: 206-543-3100.

Notes
The authors declare no competing financial interest.

■ ACKNOWLEDGMENTS

■ REFERENCES

(1) Oregan, B.; Gratzel, M. A Low-Cost, High-Efficiency Solar-Cell Based on Dye-Sensitized Colloidal TiO$_2$ Films. *Nature* **1991**, *353* (6346), 737−740.

(2) Zhang, Q. F.; Cao, G. Z. Nanostructured Photoelectrodes for Dye-Sensitized Solar Cells. *Nano Today* **2011**, *6* (1), 91−109.

(3) Zhang, Q. F.; Dandeneau, C. S.; Zhou, X. Y.; Cao, G. Z. ZnO Nanostructures for Dye-Sensitized Solar Cells. *Adv. Mater.* **2009**, *21* (41), 4087−4108.

(4) Mor, G. K.; Varghese, O. K.; Paulose, M.; Shankar, K.; Grimes, C. A. A Review on Highly Ordered, Vertically Oriented TiO$_2$ Nanotube Arrays: Fabrication, Material Properties, and Solar Energy Applications. *Sol. Energy Mater. Sol. Cells* **2006**, *90* (14), 2011−2075.

(5) Mathew, S.; Yella, A.; Gao, P.; Humphry-Baker, R.; Curchod, B. F. E.; Ashari-Astani, N.; Tavernelli, I.; Rothlisberger, U.; Nazeeruddin, M. K.; Gratzel, M. Dye-Sensitized Solar Cells with 13% Efficiency Achieved through the Molecular Engineering of Porphyrin Sensitizers. *Nat. Chem.* **2014**, *6* (3), 242−247.

(6) Hendry, E.; Koeberg, M.; O'Regan, B.; Bonn, M. Local Field Effects on Electron Transport in Nanostructured TiO$_2$ Revealed by Terahertz Spectroscopy. *Nano Lett.* **2006**, *6* (4), 755−759.

(7) Zhu, K.; Neale, N. R.; Miedaner, A.; Frank, A. J. Enhanced Charge-Collection Efficiencies and Light Scattering in Dye-Sensitized Solar Cells Using Oriented TiO$_2$ Nanotubes Arrays. *Nano Lett.* **2007**, *7* (1), 69−74.

(8) Hossain, M. A.; Jennings, J. R.; Koh, Z. Y.; Wang, Q. Carrier Generation and Collection in CdS/CdSe-Sensitized SnO$_2$ Solar Cells Exhibiting Unprecedented Photocurrent Densities. *ACS Nano* **2011**, *5* (4), 3172−3181.

(9) Dou, X. C.; Sabba, D.; Mathews, N.; Wong, L. H.; Lam, Y. M.; Mhaisalkar, S. Hydrothermal Synthesis of High Electron Mobility Zn-Doped SnO$_2$ Nanoflowers as Photoanode Material for Efficient Dye-Sensitized Solar Cells. *Chem. Mater.* **2011**, *23* (17), 3938−3945.

(10) Chen, H. Y.; Kuang, D. B.; Su, C. Y. Hierarchically Micro/Nanostructured Photoanode Materials for Dye-Sensitized Solar Cells. *J. Mater. Chem.* **2012**, *22* (31), 15475−15489.

(11) Senevirathna, M. K. I.; Pitigala, P. K. D. D. P.; Premalal, E. V. A.; Tennakone, K.; Kumara, G. R. A.; Konno, A. Stability of the SnO$_2$/MgO Dye-Sensitized Photo Electrochemical Solar Cell. *Sol. Energy Mater. Sol. Cells* **2007**, *91* (6), 544−547.

(12) Chen, W.; Qiu, Y.; Yang, S. A New ZnO Nanotetrapods/SnO$_2$ Nanoparticles Composite Photoanode for High Efficiency Flexible Dye-Sensitized Solar Cells. *Phys. Chem. Chem. Phys.* **2010**, *12* (32), 9494−9501.

(13) Chen, W.; Qiu, Y. C.; Zhong, Y. C.; Wong, K. S.; Yang, S. H. High-Efficiency Dye-Sensitized Solar Cells Based on the Composite Photoanocles of SnO$_2$ Nanoparticles/ZnO Nanotetrapods. *J. Phys. Chem. A* **2010**, *114* (9), 3127−3138.

(14) Li, N. C.; Martin, C. R.; Scrosati, B. A High-Rate, High-Capacity, Nanostructured Tin Oxide Electrode. *Electrochem. Solid-State Lett.* **2000**, *3* (7), 316−318.

(15) Kim, D. W.; Hwang, I. S.; Kwon, S. J.; Kang, H. Y.; Park, K. S.; Choi, Y. J.; Choi, K. J.; Park, J. G. Highly Conductive Coaxial SnO$_2$-In$_2$O$_3$ Heterostructured Nanowires for Li Ion Battery Electrodes. *Nano Lett.* **2007**, *7* (10), 3041−3045.

(16) Park, M. S.; Kang, Y. M.; Wang, G. X.; Dou, S. X.; Liu, H. K. The Effect of Morphological Modification on the Electrochemical Properties of SnO$_2$ Nanomaterials. *Adv. Funct. Mater.* **2008**, *18* (3), 455−461.

(17) Han, S. J.; Jang, B. C.; Kim, T.; Oh, S. M.; Hyeon, T. Simple Synthesis of Hollow Tin Dioxide Microspheres and Their Application to Lithium-Ion Battery Anodes. *Adv. Funct. Mater.* **2005**, *15* (11), 1845−1850.

(18) Zhao, Q. R.; Xie, Y.; Dong, T.; Zhang, Z. G. Oxidation-Crystallization Process of Colloids: An Effective Approach for the Morphology Controllable Synthesis of SnO$_2$ Hollow Spheres and Rod Bundles. *J. Phys. Chem. C* **2007**, *111* (31), 11598−11603.

(19) Lou, X. W.; Wang, Y.; Yuan, C. L.; Lee, J. Y.; Archer, L. A. Template-Free Synthesis of SnO$_2$ Hollow Nanostructures with High Lithium Storage Capacity. *Adv. Mater.* **2006**, *18* (17), 2325−2329.

(20) Yang, H. X.; Qian, J. F.; Chen, Z. X.; Ai, X. P.; Cao, Y. L. Multilayered Nanocrystalline SnO$_2$ Hollow Microspheres Synthesized by Chemically Induced Self-Assembly in the Hydrothermal Environment. *J. Phys. Chem. C* **2007**, *111* (38), 14067−14071.

(21) Cheng, B.; Russell, J. M.; Shi, W. S.; Zhang, L.; Samulski, E. T. Large-Scale, Solution-Phase Growth of Single-Crystalline SnO$_2$ Nanorods. *J. Am. Chem. Soc.* **2004**, *126* (19), 5972−5973.

(22) Wu, H. B.; Chen, J. S.; Lou, X. W.; Hng, H. H. Synthesis of SnO$_2$ Hierarchical Structures Assembled from Nanosheets and Their Lithium Storage Properties. *J. Phys. Chem. C* **2011**, *115* (50), 24605−24610.

(23) Qian, J. F.; Liu, P.; Xiao, Y.; Jiang, Y.; Cao, Y. L.; Ai, X. P.; Yang, H. X. TiO$_2$-Coated Multilayered SnO$_2$ Hollow Microspheres for Dye-Sensitized Solar Cells. *Adv. Mater.* **2009**, *21* (36), 3663−3667.

(24) Hossain, A.; Yang, G. W.; Parameswaran, M.; Jennings, J. R.; Wang, Q. Mesoporous SnO$_2$ Spheres Synthesized by Electrochemical Anodization and Their Application in CdSe-Sensitized Solar Cells. *J. Phys. Chem. C* **2010**, *114* (49), 21878−21884.

(25) Bilecka, I.; Niederberger, M. Microwave Chemistry for Inorganic Nanomaterials Synthesis. *Nanoscale* **2010**, *2* (8), 1358−1374.

(26) Ding, K. L.; Miao, Z. J.; Liu, Z. M.; Zhang, Z. F.; Han, B. X.; An, G. M.; Miao, S. D.; Xie, Y. Facile Synthesis of High Quality TiO$_2$ Nanocrystals in Ionic Liquid Via a Microwave-Assisted Process. *J. Am. Chem. Soc.* **2007**, *129* (20), 6362−+.

(27) Hu, X. L.; Zhu, Y. J.; Wang, S. W. Sonochemical and Microwave-Assisted Synthesis of Linked Single-Crystalline Zno Rods. *Mater. Chem. Phys.* **2004**, *88* (2−3), 421−426.

(28) Patzke, G. R.; Krumeich, F.; Nesper, R. Oxidic Nanotubes and Nanorods - Anisotropic Modules for a Future Nanotechnology. *Angew. Chem., Int. Ed.* **2002**, *41* (14), 2446−2461.

(29) Burda, C.; Chen, X. B.; Narayanan, R.; El-Sayed, M. A. Chemistry and Properties of Nanocrystals of Different Shapes. *Chem. Rev.* **2005**, *105* (4), 1025−1102.

(30) Jun, Y. W.; Choi, J. S.; Cheon, J. Shape Control of Semiconductor and Metal Oxide Nanocrystals through Nonhydrolytic Colloidal Routes. *Angew. Chem., Int. Ed.* **2006**, *45* (21), 3414−3439.

(31) Yang, R.; Gu, Y. G.; Li, Y. Q.; Zheng, J.; Li, X. G. Self-Assembled 3-D Flower-Shaped SnO$_2$ Nanostructures with Improved Electrochemical Performance for Lithium Storage. *Acta Mater.* **2010**, *58* (3), 866−874.

(32) Cao, G.; Wang, Y. *Nanostructures and Nanomaterials: Synthesis, Properties, and Applications*; World Scientific Publishing Company: Singapore, 2011.

(33) Huang, H.-L.; Cao, G. Z.; Shen, I. Y. Hydrothermal Synthesis of Lead Zirconate Titanate (PZT or Pb(Zr$_{0.52}$Ti$_{0.48}$)O$_3$) Nano-Particles Using Controlled Ramping and Cooling Rates. *Sens. Actuators, A* **2014**, *214*, 111−119.

(34) Yella, A.; Lee, H. W.; Tsao, H. N.; Yi, C. Y.; Chandiran, A. K.; Nazeeruddin, M. K.; Diau, E. W. G.; Yeh, C. Y.; Zakeeruddin, S. M.; Gratzel, M. Porphyrin-Sensitized Solar Cells with Cobalt (II/III)-Based Redox Electrolyte Exceed 12% Efficiency. *Science* **2011**, *334* (6056), 629−634.

(35) van de Lagemaat, J.; Frank, A. J. Nonthermalized Electron Transport in Dye-Sensitized Nanocrystalline TiO$_2$ Films: Transient Photocurrent and Random-Walk Modeling Studies. *J. Phys. Chem. B* **2001**, *105* (45), 11194−11205.

(36) Kim, J. Y.; Noh, J. H.; Zhu, K.; Halverson, A. F.; Neale, N. R.; Park, S.; Hong, K. S.; Frank, A. J. General Strategy for Fabricating Transparent TiO$_2$ Nanotube Arrays for Dye-Sensitized Photoelectrodes: Illumination Geometry and Transport Properties. *ACS Nano* **2011**, *5* (4), 2647−2656.

(37) Oekermann, T.; Zhang, D.; Yoshida, T.; Minoura, H. Electron Transport and Back Reaction in Nanocrystalline TiO$_2$ Films Prepared by Hydrothermal Crystallization. *J. Phys. Chem. B* **2004**, *108* (7), 2227−2235.

(38) Zhu, K.; Vinzant, T. B.; Neale, N. R.; Frank, A. J. Removing Structural Disorder from Oriented TiO$_2$ Nanotube Arrays: Reducing the Dimensionality of Transport and Recombination in Dye-Sensitized Solar Cells. *Nano Lett.* **2007**, *7* (12), 3739−3746.

25938

dx.doi.org/10.1021/jp5089146 | *J. Phys. Chem. C* 2014, 118, 25931−25938